MAGNETIC MICROWAVE DEVICES

In this article we discuss the following topics on magnetic microwave devices: yttrium–iron–garnet (YIG) film devices, magnetostatic waves, magnetooptic devices, absorbing layers, antireflection layers, and nonlinear responses. The article is organized as follows: The section entitled "Theoretical Background" presents a general theoretical background underlying the physics for the operation of ferrite components in microwave devices. Discussions include the derivation of the Polder permeability tensor, the effective fields associated with electron spin motion, the general dispersion spectrum for electromagnetic waves propagating in a bulk magnetic medium, magnetostatic waves admitted by the geometry of a YIG film, and the nonlinear instabilities for spin waves occurring at high power. The section entitled "Magnetostatic Waves and YIG Film Devices" describes YIG film devices based on the operation of magnetostatic waves (MSWs), including delay lines, filters, directional couplers, and resonators. The section entitled "Magnetic Microwave Nonlinear Devices" depicts nonlinear magnetic devices of frequency selective power limiters, signal-to-noise enhancers, amplitude correctors, and ferrimagnetic echoing devices. The section entitled "Magnetooptic Devices" discusses magnetooptic Kerr and Faraday effects and describes the operation of magnetooptic Bragg diffraction devices. Finally, design of microwave absorbing layers and antireflection layers is briefly mentioned in the section entitled "Antireflection Layers and Absorbing Layers."

THEORETICAL BACKGROUND

This section provides a theoretical background underlying the physics that allows for the operation of a magnetic microwave device. A magnetic microwave device generally requires the use of an insulating magnetic ferrite material so that magnetization or spin motion is coupled to Maxwell equations without inducing much eddy-current loss at high frequencies. Also, in order to eliminate domain wall motion, single-domain operation is preferred at radio frequencies, and the ferrite material needs to be magnetized to saturation using an external direct current (dc) magnetic field. Alternatively, effective fields arising from either the crystalline or shape anisotropy of the ferrite material may be used to fulfull the bias requirement of the magnetic device. Thus, under small-signal approximations the electromagnetic property of the ferrite is described by a tensor permeability whose off-diagonal elements result in novel applications of nonreciprocal devices, for example. Most important, the permeability tensor can be varied by adjusting the bias field strength, resulting in tunability of the microwave device over frequencies.

A magnetic microwave device is normally operating in the frequency range from 0.1 GHz to 40 GHz or higher, and its performance can be interpreted in terms of the spin/magnetization motion of the ferrite material where coupling to optical/photon modes, elastic/phonon modes, or exchange/magnon modes may be utilized. Depending on the regime of applications, a microwave magnetic device may be distinguished as either a magnetodynamic device or a magnetostatic-wave device. The first class of devices includes circulators, isolators, filters, phase shifters, patch antennas, and so on, whose operation must be analyzed using the full set of Maxwell equations. The second class consists of mainly high-quality single-crystal yttrium–iron–garnet film devices where the propagation of magnetization waves involves a wavelength comparable to the film thickness. As such, the displacement currents can be omitted in Maxwell equations. This renders the so-called magnetostatic approximation, which implies that the resultant radiofrequency RF-magnetic field can be derived from a scalar potential. Important magnetostatic devices include delay lines, filters, resonators, echo lines, and other nonlinear devices, whose operation complements their low-frequency counterparts below 2 GHz involving surface acoustic wave (SAW) devices. Magnetodynamic devices are not discussed in this article.

In the following subsections we first derive the coupling between the magnetization field and the other electromagnetic fields, giving rise to a Polder permeability tensor for the ferrite material under small-signal approximation. Effective fields are then introduced in the equation of motion, allowing for the coupling of the magnetization field with the other physical fields required for transducer applications. Based on the frequency versus wave-number dispersion diagram, the propagation of magnetization waves can be divided into three zones upon which magnetic microwave devices are conventionally defined at several regimes. Magnetostatic waves are then discussed, whose dispersion diagrams are described in terms of the bias-field configuration relative to the YIG-film device geometry. Finally, spin-wave instability is briefly mentioned, delineating the high-power threshold that a ferrite device can operate before a cascading energy transfer occurs be-

tween the input rf power and the parametric excitation of spin waves.

Polder Permeability Tensor

In a source-free medium, Maxwell equations take the form

$$\begin{aligned} \nabla \times \boldsymbol{h} &= j\omega\epsilon\boldsymbol{e}, \quad & \nabla \times \boldsymbol{e} &= -j\omega\boldsymbol{b} \\ \nabla \cdot \boldsymbol{b} &= 0, & \nabla \cdot \boldsymbol{e} &= 0 \end{aligned} \tag{1}$$

where $\boldsymbol{e}$ and $\boldsymbol{h}$ are the RF electric and magnetic fields and $\boldsymbol{b}$ is the RF magnetic induction field. In Eq. (1), ϵ denotes the permittivity and the time dependence of the RF quantities is assumed to be $\exp(j\omega t)$. For a linear isotropic medium one may define a constant μ, the permeability, so that $\boldsymbol{b}$ and $\boldsymbol{h}$ are linearly proportional to each other:

$$\boldsymbol{b} = \mu\boldsymbol{h} \tag{2}$$

Equation (2) holds true if the medium is diamagnetic ($\mu < \mu_0$) or paramagnetic ($\mu > \mu_0$). Here μ_0 denotes the permeability of vacuum. For a ferromagnetic or a ferrimagnetic medium the relationship between $\boldsymbol{b}$ and $\boldsymbol{h}$ is neither linear nor isotropic. However, under small-signal approximation the linear relationship between $\boldsymbol{b}$ and $\boldsymbol{h}$ may be assumed, but the scalar permeability needs to be replaced by a tensor. That is, Eq. (2) becomes

$$\boldsymbol{b} = \underline{\underline{\boldsymbol{\mu}}}\boldsymbol{h} = \mu_0(\boldsymbol{m} + \boldsymbol{h}) \tag{3}$$

Here, $\boldsymbol{m}$ denotes the RF magnetization field, and $\underline{\underline{\boldsymbol{\mu}}}$ is called the permeability tensor (1).

In a magnetic substance the net magnetic dipole moment per volume, or the magnetization, denoted as $\boldsymbol{M}$, is nonzero due to spontaneous magnetization of the material. Denote the angular momentum per volume of the medium be $\boldsymbol{J}$. The time rate change of angular momentum can be equated with the applied torque, and this implies

$$\frac{\partial \boldsymbol{J}}{\partial t} = \mu_0 \boldsymbol{M} \times \boldsymbol{H} \tag{4}$$

Here, $\boldsymbol{H}$ denotes the internal magnetic field within the volume. From both classical mechanics and quantum mechanics, the relationship between $\boldsymbol{J}$ and $\boldsymbol{M}$ is linear, which can be expressed as

$$\boldsymbol{M} = \gamma \boldsymbol{J} \tag{5}$$

In Eq. (5) γ is called the *gyromagnetic ratio,* which can be written as

$$\gamma = -\frac{g|e|}{2m_e} \tag{6}$$

where g is the Landé g factor, and e and m_e are charge and mass of an electron, respectively. Classically, $g = 1$, for orbital angular momentum, and $g = 2$, for spin angular momentum. Quantum mechanically, g can take a noninteger value between 1 and 2 due to the interaction between the spin and the orbital motion of the electron (2). However, for magnetic transition metal ions, Fe, Co, and Ni, the orbital motion of $3d$ electrons is usually quenched and hence $g \approx 2$. This implies $\gamma = -1.76 \times 10^{11}$ C/kg. Combining Eqs. (4) and (5), we derive, therefore, the following constitutive equation for a magnetic medium:

$$\frac{\partial \boldsymbol{M}}{\partial t} = \gamma \mu_0 \boldsymbol{M} \times \boldsymbol{H} \tag{7}$$

We now assume that the magnetic medium is magnetized to saturation either by an externally applied magnetic field or by an internal anisotropy field, or both. Let the saturation magnetization be denoted as M_S. We separate the dc and the rf components of $\boldsymbol{M}$ and $\boldsymbol{H}$ as follows:

$$\boldsymbol{M} = \boldsymbol{M}_0 + \boldsymbol{m}, \qquad \boldsymbol{H} = \boldsymbol{H}_0 + \boldsymbol{h} \tag{8}$$

Here, capital letters denote dc quantities, and lowercase denote RF quantities. Under the small-signal assumption, $|\boldsymbol{m}| \ll |\boldsymbol{M}_0| \approx M_s$, $|\boldsymbol{h}| \ll |\boldsymbol{H}_0|$, Eq. (7) can be linearized to yield

$$\frac{\partial \boldsymbol{m}}{\partial t} = \gamma \mu_0 M_S \boldsymbol{i}_z \times \left(\boldsymbol{h} - \frac{H_0}{M_S}\boldsymbol{m}\right) \tag{9}$$

In Eq. (9) we have assumed $\boldsymbol{H}_0$, and hence $\boldsymbol{M}_0$, to be along the z axis whose unit vector is denoted as $\boldsymbol{i}_z$. From Eqs. (3) and (9), we derive, assuming again the $\exp(j\omega t)$ time dependence, following the Polder tensor permeability

$$\underline{\underline{\boldsymbol{\mu}}} = \mu_0 \begin{pmatrix} \mu & -j\kappa & 0 \\ j\kappa & \mu & 0 \\ 0 & 0 & 1 \end{pmatrix} \tag{10}$$

The Polder tensor elements μ and κ are given as

$$\mu = 1 + \frac{\omega_z \omega_m}{\omega_z^2 - \omega^2} \tag{11}$$

$$\kappa = \frac{\omega \omega_m}{\omega_z^2 - \omega^2} \tag{12}$$

and ω_z and ω_m are defined as

$$\omega_z = |\gamma|\mu_0 M_S \tag{13}$$

$$\omega_m = |\gamma|\mu_0 H_0 \tag{14}$$

Equations (1), (3), and (10) sufficiently describe the general behavior of a linear microwave magnetic device.

Effective Fields

In Eq. (7) the magnetic field $\boldsymbol{H}$ is the internal field effectively experienced by the spins in the magnetic medium. In other words, an effective field is defined if there exists a coupling between the magnetization motion of the medium and the other physical field quantities. The coupling energy density is denoted as $w(\boldsymbol{M}, \partial\boldsymbol{M}/\partial x_i)$, which may show dependence on the magnetization $\boldsymbol{M}$, the magnetic strains $\partial\boldsymbol{M}/\partial x_j$, or both. For example, the externally applied magnetic field, $\boldsymbol{H}_a$, can be associated with the Zeeman energy density, $w = \mu_0 \boldsymbol{H}_a \cdot \boldsymbol{M}$. For other couplings the resultant effective fields can be derived

from the following Lagrangian equations (3,4):

$$(\boldsymbol{H}_{\text{eff}})_i = \frac{1}{\mu_0}\left[-\frac{\partial w}{\partial M_i} + \sum_{j=1}^{3}\frac{\partial}{\partial x_j}\frac{\partial w}{\partial(\partial M_i/\partial x_j)}\right], \qquad i = 1, 2, 3 \tag{15}$$

The associated energy flux is

$$s_i = \sum_{j=1}^{3}\frac{-\partial w}{\partial(\partial M_j/\partial x_i)}\frac{\partial M_j}{\partial t}, \qquad i = 1, 2, 3 \tag{16}$$

so that

$$\frac{\partial \boldsymbol{w}}{\partial t} + \nabla \cdot \boldsymbol{s} = 0 \tag{17}$$

In general, $\boldsymbol{H}$ in Eq. (7) consists of the following components:

$$\boldsymbol{H} = \boldsymbol{H}_{\text{a}} + \boldsymbol{H}_{\text{D}} + \boldsymbol{H}_{\text{A}} + \boldsymbol{H}_{\text{E}} + \boldsymbol{H}_{S} + \boldsymbol{h}_{\text{RF}} + \boldsymbol{h}_{\text{d}} + \boldsymbol{h}_{\text{G}} \tag{18}$$

where

$$\boldsymbol{H}_{\text{a}} = \text{externally applied magnetic field (parallel to the } z \text{ axis)} \tag{19}$$

$$\boldsymbol{H}_{\text{D}} = \text{dc demagnetizing field} \tag{20}$$

$$\boldsymbol{H}_{\text{A}} = (2K/\mu_0 M_{\text{S}})\boldsymbol{i}_z = \text{uniaxial anisotropy field (along the } z \text{ axis)} \tag{21}$$

$$\boldsymbol{H}_{\text{E}} = (2A/\mu_0 M_{\text{S}}^2)\nabla^2\boldsymbol{M} = \text{magnetic exchange field} \tag{22}$$

$$\boldsymbol{H}_{S} = \text{magnetoelastic field} \tag{23}$$

$$\boldsymbol{h}_{\text{RF}} = \text{externally applied RF driving field} \tag{24}$$

$$\boldsymbol{h}_{\text{d}} = \text{RF dipolar field} \tag{25}$$

$$\boldsymbol{h}_{\text{G}} = (-\lambda/\gamma\mu_0 M_{\text{S}})\partial\boldsymbol{M}/\partial t = \text{Gilbert damping field} \tag{26}$$

$\boldsymbol{K}$, $\boldsymbol{A}$, and λ are, respectively, the (uniaxial) anisotropy constant, exchange stiffness, and Gilbert damping constant. We note that although $\boldsymbol{H}_{\text{A}}$, $\boldsymbol{H}_{\text{E}}$, and $\boldsymbol{H}_{S}$ are written in capital letters, they may contain both dc and RF components.

The dc demagnetizing field, $\boldsymbol{H}_{\text{D}}$, which results from the shape anisotropy, can be solved analytically only for an ellipsoidally shaped body. In this case a demagnetizing-factor tensor $\underline{\underline{\mathbf{N}}}_{\text{D}}$ can be calculated so that (1)

$$\boldsymbol{H}_{\text{D}} = -\underline{\underline{\mathbf{N}}}_{\text{D}}\boldsymbol{M}_0 \tag{27}$$

where $\boldsymbol{M}_0$ denotes the dc component of the magnetization expressed in Eq. (8). For the limiting case of a thin flat ferrite slab lying on the x–y plane, Eq. (27) becomes

$$\boldsymbol{H}_{\text{D}} = -\boldsymbol{M} \cdot \boldsymbol{e}_z\boldsymbol{e}_z \tag{28}$$

Equation (21) denotes the effective field associated with a uniaxial anisotropy. For other anisotropy fields, $\boldsymbol{H}_{\text{A}}$ can be derived from Eq. (15) using the appropriate energy density of the anisotropy. For example, the corresponding energy density for a cubic anisotropy is

$$w_{\text{A}} = K_1(\alpha_1^2\alpha_2^2 + \alpha_2^2\alpha_3^2 + \alpha_3^2\alpha_1^2) + K_2\alpha_1^2\alpha_1^2\alpha_1^2 + \cdots \tag{29}$$

where α_i, $i = 1, 2, 3$, is the directional cosine of the magnetization, $\boldsymbol{M}$, with respect to the ith cubic axis, and K_1 and K_2 are the associated anisotropy constants (5).

By using Eq. (15) the magnetoelastic field can be derived from the following magnetoelastic energy density

$$\begin{aligned} w_S = {} & b_1(\alpha_1^2\epsilon_{11} + \alpha_2^2\epsilon_{22} + \alpha_3^2\epsilon_{33} \\ & + 2b_2(\alpha_1\alpha_2\epsilon_{12} + \alpha_2\alpha_3\epsilon_{23} + \alpha_3\alpha_1\epsilon_{31}) \end{aligned} \tag{30}$$

where α_i, $i = 1, 2, 3$, is the directional cosine of the magnetization, $\boldsymbol{M}$; ϵ_{ij}, $i, j = 1, 2, 3$, is the strain field, and b_1 and b_2 are the magnetoelastic coupling constants (3). The magnetoelastic coupling measures the response that a strain signal or an acoustic signal is converted into a magnetic signal in a magnetoelastic transducer device, or vice versa.

The dipolar field $\boldsymbol{h}_{\text{d}}$ denotes the RF field associated with the RF magnetization field $\boldsymbol{m}$ in Eq. (8), which needs to be solved from Maxwell equation, Eq. (1). When expressed in the spectral domain $\boldsymbol{h}_{\text{d}}$ relates to $\boldsymbol{m}$ as follows:

$$\boldsymbol{h}_{\text{d}} = (\underline{\underline{\boldsymbol{\mu}}}/\mu_0 - \underline{\underline{\mathbf{I}}})^{-1}\boldsymbol{m} \tag{31}$$

where $\underline{\underline{\boldsymbol{\mu}}}$ is the Polder tensor derived earlier in this section and $\underline{\underline{\mathbf{I}}}$ denotes the identity tensor. Under magnetostatic approximation, $\boldsymbol{h}_{\text{d}}$ satisfies the following magnetostatic equations

$$\nabla \cdot \boldsymbol{h}_{\text{d}} = -\nabla \cdot \boldsymbol{m} \tag{32}$$

$$\nabla \times \boldsymbol{h}_{\text{d}} = 0 \tag{33}$$

subject to suitable boundary conditions. Thus, $\boldsymbol{h}_{\text{d}}$ is solved from $\boldsymbol{m}$ in almost the same way that the dc demagnetizing field $\boldsymbol{H}_{\text{D}}$ is solved from $\boldsymbol{M}_0$. In the literature $\boldsymbol{h}_{\text{d}}$ is sometimes called the RF demagnetizing field.

The Gilbert damping field can be effectively accounted for if one replaces H_0 in Eq. (8) by $H_0 + (j\lambda/\gamma\mu_0)\omega$, or, equivalently (1),

$$H_0 \to H_0 + \frac{j\Delta H}{2} \tag{34}$$

where ΔH denotes the ferromagnetic resonance (FMR) linewidth. The Gilbert damping term is identical to the Landau–Lifshitz form in first order, which is introduced into the equation of motion, Eq. (7), phenomenologically to account for the damping torque experienced by the spins undergoing precessing motion. Equation (34) describes the measured magnetic loss of a magnetic microwave device very well, provided that the applied RF frequency is not too different from the frequency that ΔH was measured. However, the physical meaning of the Gilbert damping, as related to the relaxation processes in the medium, is lacking, in contrast with the other damping forms—for example, the Bloch–Bloembergen damping (1).

Finally, we have to specify the boundary conditions on $\boldsymbol{m}$ in the presence of an exchange field given by Eq. (22). The (direct) exchange coupling is associated with the overlapping integral which relates the spin–spin interaction for two electron spins at neighboring atomic sites. The exchange constant A is larger than 0 for ferromagnetic coupling, and A is smaller than 0 for ferrimagnetic and for antiferromagnetic couplings. The spatial boundary condition on $\boldsymbol{m}$ can be derived from the

equation of motion, Eq. (7), which requires that the quantity

$$\mu_0 AM \times \frac{\partial \boldsymbol{M}}{\partial n} \tag{35}$$

needs to be continuous across the ferrite boundaries. Here $\boldsymbol{n}$ denotes the direction normal to the outward surface of the boundary. The time boundary condition is derived from the energy conservation law. That is, from Eq. (16) we require the outward energy flux

$$-\mu_0 A \frac{\partial \boldsymbol{M}}{\partial n} \cdot \frac{\partial \boldsymbol{M}}{\partial t} \tag{36}$$

to be continuous across the material boundaries. However, instead of Eq. (36), it is popular in the literature to use the following spin-pinning condition at the material boundaries:

$$\frac{\partial \boldsymbol{M}}{\partial t} = 0 \tag{37}$$

Since A is a microscopic quantity and at the boundary layers the environment there is quite different from that of the bulk, the pinning condition, Eq. (37), might be more realistic than the one representing the macroscopic average, Eq. (36).

Dispersion Curves for Bulk Modes

Equations (1), (3), and (10) can now be solved for a bulk ferrite medium for plane wave solutions. The resultant dispersion relation, ω versus k ($= 2\pi/\lambda$), is shown in Fig. 1. Here, k is the wave number and λ is the wavelength. In Fig. 1 the k-space is conventionally divided into three zones. For the small-k region, $k < k_1$ (≈ 0.1 cm^{-1}), electron spin motion is strongly coupled with the RF electromagnetic fields so that the full set of Maxwell equations is required to solve the dispersion relations. This region is called the *retarded zone* or *magnetodynamic zone*, and most magnetic microwave devices making use of bulk ferrite materials are operational in this region—for example, circulators, isolators, phase shifters, resonators, and so on. The next region comprises of intermediate k values, k_1 (≈ 0.1 cm^{-1}) $< k < k_2$ ($\approx 10^6$ cm^{-1}), known as the *magnetostatic wave zone.* In this region $\omega \ll k(\epsilon\mu_0)^{-1/2}$ and hence the displacement current, $\omega\epsilon\boldsymbol{e}$, can be ignored in Maxwell equations. That is

$$\nabla \times \boldsymbol{h} \approx 0 \tag{38}$$

Equation (38) is called the *magnetostatic approximation.* A magnetostatic wave device usually require the use of a high-quality single-crystal magnetic film such as YIG whose thickness determines the wavelength of the resultant magnetostatic waves prevailing in the device structure. The last region is for $k > k_2$ ($\approx 10^6$ cm^{-1}), which is called the *spin wave zone.* In this region the dispersion curves grow proportional to k^2, as dictated by the effective exchange field, $\boldsymbol{H}_E$, in Eq. (22). Although not many practical microwave devices are designed in this region, the spectrum of spin waves is important in the sense that the normal spin precessing motion will break up into spin waves at the onset of instability when a magnetic microwave device is driven beyond a high power threshold.

For a given wave propagation direction, k, Eqs. (1), (3), and (10) imply two plane wave solutions. Similar to the plane wave solutions in an isotropic medium, the three vectors, $\boldsymbol{e}$, $\boldsymbol{b}$, and $\boldsymbol{k}$, for each mode in an anisotropic magnetic medium are still mutually perpendicular to each other. However, unlike the isotropic case, the two modes in the magnetic medium are nondegenerate, possessing different effective permeabilities and polarizations. Due to the wrong sense in polarization, one mode is weakly coupled to the photon waves, and hence its dispersion curve represents little departure from that of the (uncoupled) photon modes. This dispersion curve is shown in Fig. 1 as a straight (short-) dashed line in the retarded zone. The other mode couples strongly to the photon waves, giving rise to distortion of the dispersion curves in the retarded zone.

For the strongly coupled mode, two branches show up, depending on whether the bias magnetic field is applied above or below FMR. These two branches are shown in Fig. 1 as lower and upper curves, respectively. The upper branch, curve (3) in Fig. 1, lies entirely in the retarded zone and shows very little variation with respect to the wave propagation directions. That is, the propagation of strongly coupled electromagnetic waves biased below FMR is nearly isotropic in the magnetic medium. However, the lower branch, curves (1) and (2), depends strongly on the wave propagation directions. When $\boldsymbol{k}$ is parallel to the z axis, the dispersion curve is shown as curve (1) in Fig. 1; and when $\boldsymbol{k}$ is perpendicular to the z axis, the dispersion curve is shown as curve (2). For other propagation directions, the dispersion curves are distributed between these two curves, and for this reason the region bounded by curves (1) and (2) in Fig. 1 is usually referred to as the *spin-wave manifold.* In the literature, curve

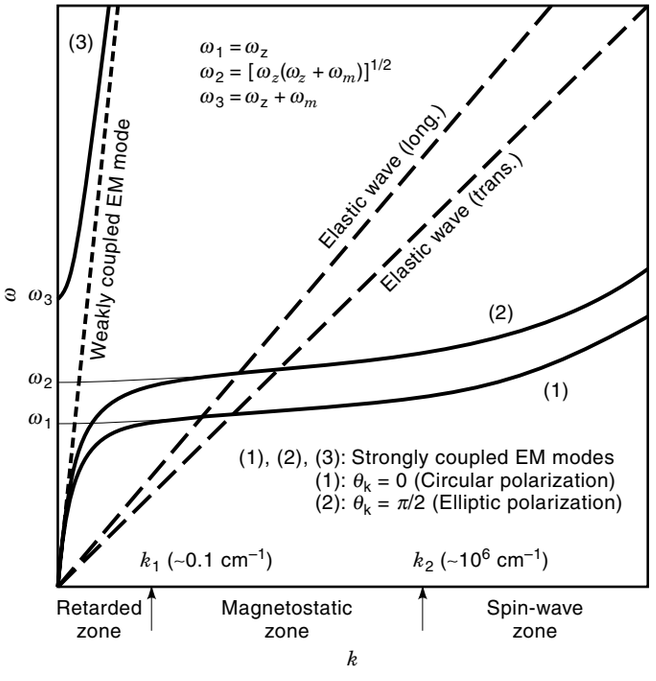

Figure 1. Dispersion curves of the coupled photon–magnon modes. The k space has been divided in three zones for retarded, magnetostatic, and spin wave modes. Phonon dispersion curves are also shown in the figure.

(1) is known as the *Kittel mode* and curve (2) is known as the *Voigt mode*. A Kittel mode possesses right-hand circular polarization, whereas a Voigt mode is associated with elliptic polarization. In Fig. 1, θ_k denotes the angle between $\boldsymbol{k}$ and the z axis, which is designated as the applied field direction, ω_1, ω_2, and ω_3 are given as

$$\omega_1 = \omega_z \tag{39}$$

$$\omega_2 = [\omega_z(\omega_z + \omega_m)]^{1/2} \tag{40}$$

$$\omega_3 = \omega_z + \omega_m \tag{41}$$

and ω_1 and ω_2 are the limiting values of the magnetostatic modes in the retarded zone.

The elastic modes are also shown in Fig. 1 as straight (long-) dashed lines. There are two kinds of phonon modes, longitudinal phonons and transverse phonons (6). In the presence of magnetoelastic coupling, b_1 and b_2 are nonzero in Eq. (30), and the phonon or acoustic modes will couple to the spin-wave, or magnon, modes. For the coupled case the dispersion curves of the phonons and the magnons will avoid running across each other in the same fashion that the photon modes and the magnon modes detour each other in the retarded zone region as shown in Fig. 1 (7). (If one views the uncoupled dispersion lines of two modes as two intersecting straight lines, the coupled dispersion lines resemble the two branches of a hyperbola using the two original lines as asymptotes.) In Fig. 1 the uncoupled magnon modes in the retarded zone are shown as dotted lines, extending curves (1) and (2) smoothly from the magnetostatic wave zone, intersecting the photon line, and ending at ω_1 and ω_2 of the ω axis.

Magnetostatic Waves in a Magnetic Layer

Wave propagation and dispersion in a magnetic layer can be derived in a manner similar to that in Fig. 1 except that boundary conditions need to be considered at the layer/air interfaces. For most device applications the excited waves have wavelengths on an order comparable to the layer thickness. As such, the magnetostatic approximation, Eq. (38), applies, which implies that the RF-magnetic field can be derived from a scalar potential, and hence the dispersion calculations are greatly simplified. Figure 2 shows such a dispersion diagram. When compared with Fig. 1, we see that the retarded zone has been pushed away into the $k = 0$ line in Fig. 2, and the exchange coupling showing k^2 dependence in the large-k region has been neglected. However, the magnetostatic dispersion is not a horizontal line, as depicted in the magnetostatic-wave zone of Fig. 1. The finite curvature of the dispersion curves shown in Fig. 2 is due to the finite thickness of the magnetic layer, d, which is distributed roughly in the region bounded by the two vertical lines $k = 0$ and $k = 2\pi/d$.

Magnetostatic waves can be volume waves and surface waves. For a volume wave the RF magnetization varies sinusoidally along the thickness direction, whereas for a surface wave it varies exponentially in this direction. Thus, a volume wave penetrates the whole thickness of the magnetic layer, whereas a surface wave is concentrated near the surface and the film-substrate interface. For a forward wave the dispersion increases monotonically with k so that the group velocity, $d\omega/dk$, is positive. This is in contrast with a backward wave where $d\omega/dk$ is negative. Thus, for a forward wave the transmitted power is along the same direction as wave propagation, whereas the power transmitted by a backward wave is opposite to the wave propagation direction.

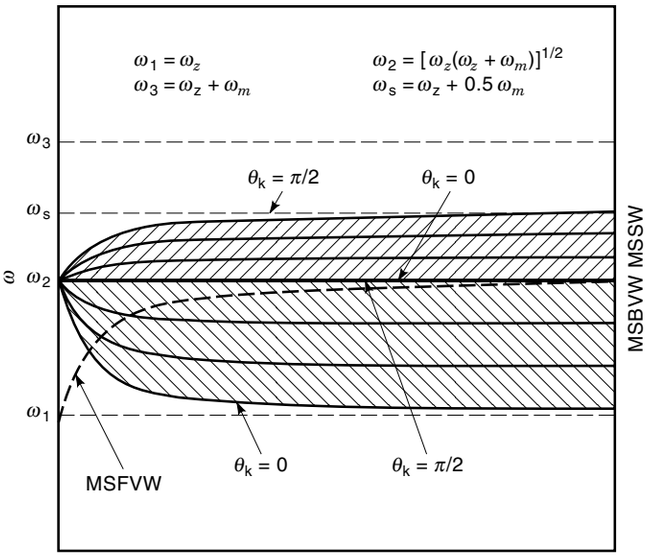

Figure 2. Dispersion curves of magnetostatic waves in a magnetic layer. The MSFVW is shown as a heavy dotted line, rising from ω_1 to ω_2 as k increases from 0 to ∞. The MSBVW and MSSW are shown hatched depending on the propagation direction of the magnetostatic waves. θ_k denotes the angle between the wave propagation direction and the applied field direction.

When the external field is applied normal to the layer plane, magnetostatic waves will propagate isotropically with the wave propagation direction lying on the layer plane. This branch of waves is called *magnetostatic forward volume waves* (MSFVWs), whose dispersion is shown in Fig. 2 as a heavy dotted line. The MSFVW mode undergoes uniform precessing motion at the Kittel frequency ω_1 for $k = 0$, and the frequency increases thereafter, approaching the bulk limit of the Voigt frequency ω_2 as k goes to infinity. Dispersion of this kind can be readily understood based on the spin motion occurring in the layer.

However, when the external bias field is applied in the layer plane, anisotropy results in general except at $k = 0$ where the uniform processing motion occurs at the Voigt frequency ω_2. When k increases further, two kinds of modes are possible: magnetostatic backward volume waves (MSBVWs) and magnetostatic surface waves (MSSWs). Depending on the propagation angle θ_k, MSBVW dispersion will decrease as k increases, approaching the respective bulk-mode limit as k goes to infinity. Therefore, unlike MSFVW, MSBVW occupies a finite area in the dispersion diagram, which is shown hatched between ω_1 and ω_2 in Fig. 2. For device applications, MSBVW is usually generated at $\theta_k = 0$, i.e., the excited MSBVW is collinear with the applied field direction, since it provides the widest frequency bandwidth among all the MSBVW propagation directions.

For MSSW the dispersion falls within the forbidden area of the bulk modes extending from ω_2 to ω_3 (see Figs. 1 and 2). MSSW frequencies increase as k increases, reaching limiting values at large k. The propagation of MSSW is anisotropic; and the largest frequency occurs at $\theta_k = \pi/2$, which gives rise

to a limiting frequency $\omega_s = \omega_z + 0.5\,\omega_m$, known as the *Damon and Eshbach frequency*. The most popularly used MSSW is for $\theta_k = \pi/2$, which requires the MSSW to propagate transverse to the applied field direction and results in the widest frequency band for MSSW device applications.

In Fig. 2, MSFVW and MSBVW are shown only for the lowest-order volume modes. Higher-order volume waves are also possible. A high-order volume wave, which assumes additional nodal points along the thickness of the magnetic layer, will converge to the same frequency as the lower-order waves at large k, except that the curvature of the dispersion curve is reduced. In general, magnetostatic waves are generated in single-crystal YIG films epitaxially grown on gadolinium–gallium–garnet (GGG) substrates. Very often, a dielectric superstrate, for example, alumina, is covered on top of the YIG film to facilitate the excitation of magnetostatic waves. For these applications the dispersion diagram of Fig. 2 remains qualitatively unchanged. However, when a metal ground plane is placed on top of the superstrate shown in Fig. 3 the dispersion of MSSW, but not MSFVW and MSBVW, will change. The influence of a metal plane is that the MSSW dispersion curve will grow in a convex manner, increasing initially from ω_2 at $k = 0$ to a maximum value less than ω_3 followed by decreasing to ω_s as k goes to infinity. When a second metal ground plane is added to the bottom side of the GGG substrate shown in Fig. 3 the propagation of MSSW becomes even nonreciprocal. That is, the dispersion curve is different depending on whether the wave propagation is along the $+k$ or the $-k$ direction. In Fig. 3, magnetostatic waves may be excited by using a microstrip line, consisting of only the top ground plane, or a stripline, consisting of both the top and the bottom ground planes. For a multilayered system containing alternating magnetic and dielectric layers, the bulk and the surface modes form a band structure in almost the same way that atomic energy levels are crowded into energy bands when atoms are brought together to form a periodic lattice (8,9).

Finally, let us discuss the propagation loss of a delay line. When an observer is traveling with the wave down the delay line for a delay time $t = \tau_d$, the electric field is

$$\boldsymbol{e} = \boldsymbol{e}_0 \exp[2\pi j(f + j\Delta f)\tau_g] \tag{42}$$

where $\boldsymbol{e}_0$ denotes the initial amplitude at $t = 0$. This implies that the propagation loss in decibels is

$$\alpha = 40\pi(\log_{10} e)\Delta f \tau_g \tag{43}$$

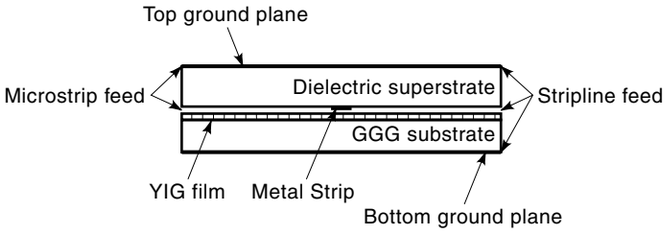

Figure 3. Magnetostatic wave excitation configuration. The YIG film is deposited on top of the GGG substrate. A superstrate can be used to provide microstrip excitation configuration. A bottom ground plane can also be deposited on the GGG substrate to provide stripline excitation configuration.

In Eq. (42), f and Δf denote the real and the imaginary part of frequency. Δf can be related to the linewidth of the device to be used as a resonator cavity weakly coupled by a feeder line circuit. Thus, we have

$$\Delta f = \Delta f_m + \Delta f_d + \Delta f_c \tag{44}$$

where Δf_m, Δf_d, and Δf_c denote, respectively, contributions from magnetic loss, dielectric loss, and conductor loss. As discussed in deriving Eq. (34), Δf_m may be identified as half the FMR linewidth multiplied by a volume filling factor F_m denoting the volume ratio of the ferrite material relative to the total volume enclosing the resonating cavity:

$$\Delta f_m = F_m |\gamma| \mu_0 \Delta H/2 \tag{45}$$

The other two linewidths Δf_d and Δf_c can be estimated in a normal way dealing with a dielectric loss cavity (see, for example, Ref. 10). If we assume that magnetic loss dominates and approximate $F_m \approx 1$, Eqs. (43) and (45) imply

$$\alpha \approx 76.4 \tau_d \Delta H \tag{46}$$

where τ_d is in microseconds and ΔH is in oersteds. Equation (46) was originally derived in Ref. 11 for an MSW delay line. However, since delay time is measured as group delay, τ_d expressed in Eqs. (42), (43), and (46) shall be multiplied by a factor v_g/v_k, where v_g denotes the group velocity ($= d\omega/dk$) and v_k denotes the phase velocity ($= \omega/k$) for wave propagation.

Spin-Wave Instability

Finally, let us discuss briefly the spin-wave instability occurring at the high power threshold of a magnetic microwave device (12). The spectrum of spin waves shown in Fig. 1 has proved to play a dominant role in the relaxation processes. When an RF field is applied, it drives the spins into precessing motion, which in turn couples with spin-wave propagation, dumping energy into lattice vibration via spin–spin and spin–lattice relaxation processes. The coupling to spin waves must originate from the nonlinear terms in the equation of motion, Eq. (7). The second-order terms come from $\boldsymbol{h} \times \boldsymbol{m}$ and the third-order terms come from either $\boldsymbol{hm} \cdot \boldsymbol{m}$ or $\boldsymbol{mm} \cdot \boldsymbol{m}$. For a spin-wave component, $\boldsymbol{m}_k$, it generates two accompanying $\boldsymbol{h}$ fields, the RF exchange field, denoted as $\boldsymbol{h}_E$, from Eq. (22), and the dipolar field, $\boldsymbol{h}_d$, from Eqs. (32) and (33). These two $\boldsymbol{h}$ fields then feed back and couple nonlinearly with the original $\boldsymbol{m}_k$ field to generate instability if a threshold power is reached. The $\boldsymbol{m} \cdot \boldsymbol{m}$ term arises from the constraint that the magnitude of $\boldsymbol{M}$ needs to be a constant (equal to $\boldsymbol{M}_S$). That is, in Eq. (8) the longitudinal component $\boldsymbol{M}_0$ is replaced by

$$M_0 \approx M_S(1 - \boldsymbol{m} \cdot \boldsymbol{m}/2M_s^2) \tag{47}$$

As a consequence, the dc demagnetizing field, if not zero, will add cubic nonlinearity to the equation of motion, giving rise to adverse effects in influencing the spin-wave instability.

Under FMR measurements, the experiments showed a subsidiary absorption at high excitation power which occurs at a dc field less than that required by the resonance condition. Also, as the input power increases, the resonance absorption peak broadened accordingly, rendering premature

saturation of the main resonance. Suhl (12) showed that the subsidiary peak arises from a spontaneous transfer of energy from the uniform precessing motion of spins to spin waves of half the resonance frequency, $\omega_k = \omega/2$. This first-order instability is caused by the second-order interaction between the dipolar field, $\boldsymbol{h}_d$, and the spin wave, $\boldsymbol{m}_k$. The second-order instability responsible for the broadened and declined saturation of the main resonance peak comes from a catastrophic energy transfer from the uniform precessing motion of spins to spin waves of the same resonance frequency, $\omega_k = \omega$. This instability is brought about by the third-order interaction between the exchange field $\boldsymbol{h}_E$ and the spin waves, $\boldsymbol{m}_k$ and $\boldsymbol{m}_k$. The resultant input field thresholds for these two instabilities are, respectively,

$$h_d^{th} = \frac{2\Delta H_k}{\omega_m}\sqrt{(\omega - \omega_z)^2 + \omega_{\Delta H}^2} \tag{48}$$

$$h_{Ex}^{th} = h_d^{th}\sqrt{\frac{\omega_m}{2\omega_{\Delta H}}} \tag{49}$$

In Eqs. (48) and (49)

$$\omega_{\Delta H} = |\gamma|\mu_0\Delta H \tag{50}$$

and ΔH_k is the linewidth of the spin wave which is introduced phenomenologically to parameterize the energy transfer from the spin wave $\boldsymbol{m}_k$ to lattice vibration. Since $\omega_m \gg \omega_{\Delta H}$, it implies

$$h_{Ex}^{th} \gg h_d^{th} \tag{51}$$

as we expect.

MAGNETOSTATIC WAVES AND YIG FILM DEVICES

There exists continuing demand for signal processing devices which can be used for radar detection, electronics communication, and instrumentation applications. At UHF frequencies, surface acoustic wave (SAW) devices have been widely used, providing phase shifting, time delaying, and other analog signal processing functions. However, at higher frequencies above 2 GHz, SAW devices are inefficient due to device fabrication and increased insertion loss. At microwave or even millimeter wave frequencies, signal processing devices have been largely achieved utilizing the newly developed magnetostatic wave (MSW) technology providing similar functional performance as SAW devices. Additional advantages include low insertion loss, large bandwidth up to 1 GHz, ease of fabrication, frequency tuning, dispersion shaping, and nonlinear operation.

In contrast to SAWs, MSWs are very dispersive and they can be controlled easily by means of an external magnetic field. In principle, three basic types of MSWs are distinguished: forward volume MSWs (MSFVWs), backward volume MSWs (MSBVWs), and surface MSWs (MSSWs). An MSFVW is excited in the ferrite material, usually a YIG film, magnetized perpendicularly to the film plane. An MSBVW is excited in a YIG film and the magnetization direction is in the film plane along the wave propagation direction. An MSSW is also associated with a transverse magnetization, but the wave propagation is perpendicular to the direction of magnetization. All of these three types of MSWs can be effectively used in fabricating microwave devices, such as delay lines, tunable filters, phase shifters, resonators, noise suppressers, amplitude correctors, and so on.

In order to reduce wave propagation loss, high-quality single-crystal yttrium–iron–garnet (YIG) films are usually used for the fabrication of MSW devices. When YIG single-crystal films are epitaxially grown on gadolinium–gallium–garnet (GGG) substrates, the ferromagnetic resonance (FMR) linewidth, ΔH, can be as narrow as 0.3 Oe at 9 GHz, and 0.6 Oe at 20 GHz. Using Eq. (46) the propagation loss in an MSW delay line is 23 and 46 dB per microsecond at 9 and 20 GHz, respectively. Therefore, for a typical delay line application, the propagation loss requiring 200 ns delay will be, respectively, 4.6 and 9.2 dB at 9 and 20 GHz. This compares very favorably with other kinds of delay lines such as a coaxial cable; at 9 GHz a 200 ns coaxial cable would require a length of 50 m, resulting in 30 dB loss in propagation.

MSWs are excited within YIG films using either the microstrip or the stripline transducer circuits. Due to the coupling between the guided electromagnetic modes of the transducers and the spin waves in the YIG films, magnetostatic waves are generated, traveling down from the input to the output transducer to perform signal processing functions, for example. In addition to straight microstrip/stripline transducers, meander lines, gratings, and interdigital and unidirectional transducers can also be effectively used to couple in and out the MSW signals. Short-circuited and open-circuited microstrip transducers are commonly used for wideband MSW device applications. The entire MSSW, MSFVW, or MSBVW frequency band can be excited by using narrow (10 μm) microstrip transducers. For narrowband devices, meander lines and gratings can be used. These transducers can be designed with 50 to 75 Ω input impedance over wide frequency bands, and matching circuits can be used to reduce mismatch losses.

In order to reduce spurious reflection of MSWs from the YIG film edges, MSW terminations or absorbers need to be utilized. These terminations can appear in the form of ferrite powders, or iron/permalloy rods, or even recording tapes, or GaAs thin films may be placed at the YIG edges. However, the simplest way to avoid MSW interference is to cut the YIG edges into angles other than 90° such that the reflected beam is directed away from the active area of the MSW device (13). Among many MSW applications we will briefly discuss in this section the operation of MSW delay lines, filters, directional couplers, and resonators. Other nonlinear and magnetooptic MSW devices will be discussed in the sections entitled "Magnetic Microwave Nonlinear Devices" and "Magnetooptic Devices," respectively.

MSW Delay Lines

Figure 4 shows the commonly used flip-over configuration for MSW delay lines. Microstrip lines serving as the transmitter and receiver for MSWs are fabricated using a photolithographic technique on top of a dielectric superstrate such as alumina, sapphire, fused silica, or duroid material. The high-quality crystal YIG film epitaxially grown on GGG substrate is brought in contact with the transducers via a spacer layer, and the overall dielectric/spacer/YIG/GGG assembly is placed between the poles of the biasing magnet. The biasing mag-

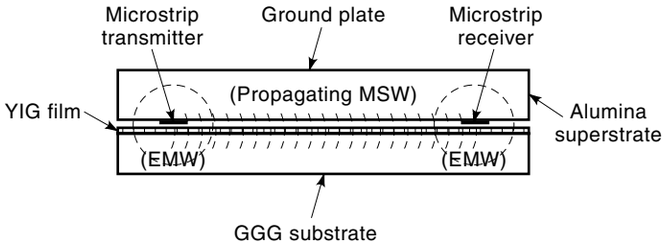

Figure 4. Schematic showing the MSW delay line configuration. Microstrip transducers are used to couple in and out the MSWs. Depending on the direction of the bias magnetic field, all types of MSWs can be excited and detected using the present circuit configuration.

netic field can be directed on the YIG film plane either parallel to or perpendicular to the microstrip lines, or perpendicular to the YIG film plane, to provide MSBVW, MSSW, or MSFVW delay line operation, respectively. Therefore, due to the coupling between the electromagnetic waves (EMWs) induced by the microstrip lines and the MSWs, the microstrip transmitter will excite MSWs which travel down the delay line structure to be picked up by the microstrip receiver. Let the distance between the transmitter and the receiver be D, and thus the time delay for this device is

$$\tau_d = D/v_g \tag{52}$$

where $v_g = d\omega/dk$ denotes the group delay velocity of MSWs.

Delay line elements exhibiting a linear dependence of the delay time, τ_d, on frequency are key components in pulse compression radar, microscan receiver, and Fourier transform systems. In general, τ_d is highly dispersive, depending nonlinearly on frequency. Various methods exist that allow τ_d to show linear dependence on frequency over wide-frequency bands (14–17). For example, at X-band it is possible to show 1 GHz bandwidth for a linearly dispersion delay line by using a thin YIG film with thickness 20 μm covered with a thin dielectric superstrate of the same thickness (14). Alternatively, the linear dependence of τ_d can be obtained by varying the separation distance between the ground plane and the YIG film (15), using the bias field gradients (16), or deploying multiple YIG films (17).

Nondispersive wideband delay lines are potential devices replacing phase shifters at microwave frequencies, providing electronic tuning capability for phased array antenna and other signal processing component applications. Therefore, we require the time delay, τ_d, to be independent of the bias field strength and, hence, the frequency over a wide frequency bandwidth. A possible solution to this requirement is to cascade two wideband linearly dispersive delay lines with opposite propagation characteristics. That is, the first device operates for forward volume MSWs and the second device operates for backward MSWs such that they compensate for each other to provide nondispersive dependence on frequencies. Other methods make use of nonuniform bias field (16) and multilayer structure (17), as discussed for the construction of a linearly dispersive delay line device.

MSW Filters

Filtering of electronic signals is performed as a frequency-selective process realized in the frequency domain. In principle, any delay line configuration can be viewed as a frequency filter structure provided that the following features are emphasized: low insertion loss occurring at the passband and high attenuation occurring at the stop bands. The filter characteristics can be feasibly obtained by controlling the transducer dimensions and the YIG/ground plane separation. While short-circuited straight microstrip lines are generally used as transducers for a wideband filter, multielement grating transducers, such as those shown in Fig. 5, are used to synthesize narrowband filters. As such, narrowband filters of bandwidth 30 MHz tunable from 3 to 7 GHz have been successfully demonstrated (18). Similarly, by carefully adjusting the width of the short-circuited microstrip transducer and the YIG film thickness, one can obtain a wideband filter tunable from 0.3 to 12 GHz with stopband rejection better than 45 dB (19). The advantage of using an MSW filter is that the passband can be tuned by varying the strength of the bias magnetic field.

MSW Directional Couplers

Figure 6 shows the schematic of an MSW directional coupler. In Fig. 6, two YIG films are deployed face to face, separated by a dielectric spacer. Ground planes are deposited on the outer sides of the GGG substrates and two multistrip lines are used as transducers, coupling in and out microwave power though exchange of MSWs. By careful design of the microstrip line-spacing as well as the dimension of the dielectric spacer, the characteristic of a directional coupler can be obtained. Operation at full power coupling is possible (20), and hence the directional coupler can be equivalently used as a bandpass filter. Also, by varying the bias field strength the power transferring coefficient of the directional coupler can be consequently adjusted.

MSW Resonators

Although the MSW bandpass filters discussed above are useful for many applications, there are occasions which require

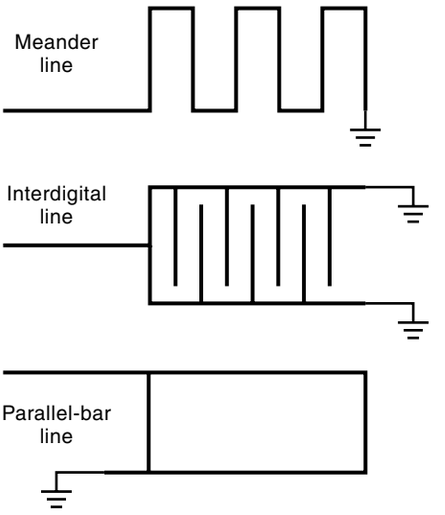

Figure 5. Microstrip circuit showing the geometry for multielement grating transducers used for excitation and receiving MSWs over a narrow frequency band for tunable filter applications.

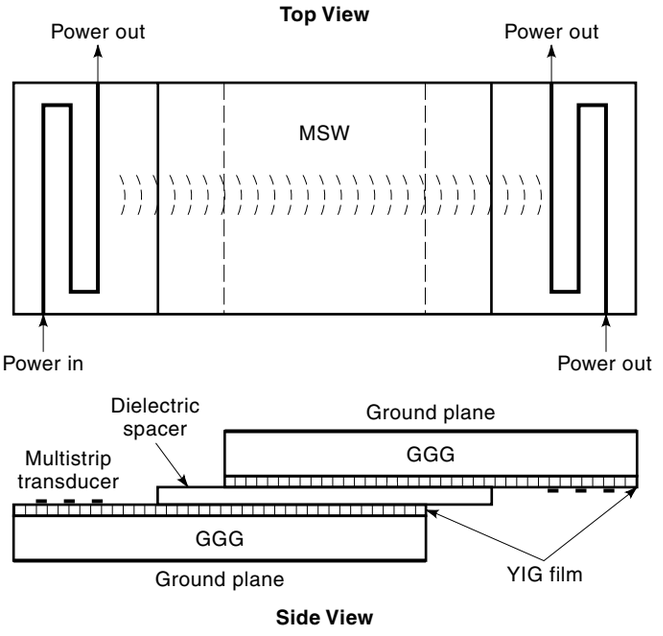

Figure 6. Schematic showing the MSW directional coupler configuration. Microstrip multistrip transducers are used to couple in and out the MSWs. All types of MSWs are possible depending on the bias field direction. The coupling coefficient between the input and output ports can be varied by changing the strength of the bias magnetic field.

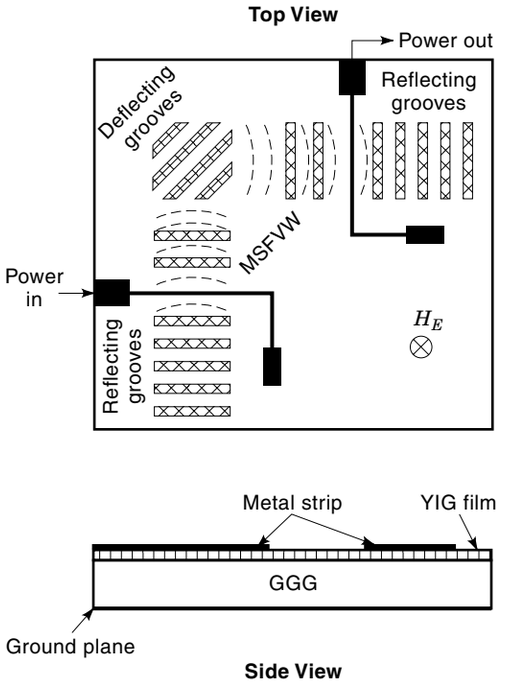

Figure 8. Schematic showing the configuration of an MSFVW resonator. Two cavities are placed at a 90° angle, which are coupled via MSFVWs passing through an obliquely oriented groove grating array. The bias field is applied perpendicular to the YIG film plane.

considerable signal selectivity over as narrow as possible a passband width. For example, tunable MSW resonators can be used as the frequency-selective elements in tunable oscillator circuits in the microwave frequency bands. MSSW resonators can be constructed by placing reflective metal gratings at the edges of the resonating cavity. Alternatively, grooves may be cut on the YIG film surface using wet etching or ion bombardment to form an MSSW cavity. This is shown in Fig. 7, in which two arrays of straight grooves are etched parallel to

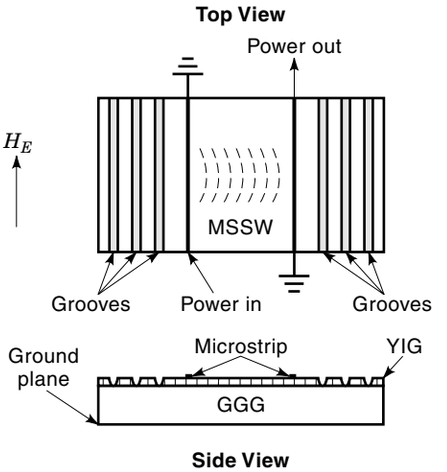

Figure 7. Schematic showing the configuration of an MSSW resonator. Reflecting arrays of grooves are cut on the YIG film surface to form an MSSW cavity resonator. The bias field is applied parallel to the microstrip transducer direction.

but on the two sides of the microstrip transducer lines; and MSSWs, once generated, bounce back and forth indefinitely between these two groove arrays at resonance. As reported in Ref. 21, MSSW resonators fabricated in this manner have shown a tuning capability between 2 GHz and 5 GHz, exhibiting a loaded Q of 500 and an off-resonance rejection level of 15 dB.

For MSFVWs the bias magnetic field is perpendicular to the YIG film plane, and hence the propagation of MSFVWs is isotropic in all the directions in the film plane. As such, the MSSW resonator shown in Fig. 7 is not suitable for MSFVW applications; it will result in poor off-resonance isolation, since at off-resonance the propagation of MSFVWs at slightly tilted angles may still satisfy the resonance condition. To avoid this drawback, a new configuration which involves two cavities coupled by MSFVWs was proposed in Ref. 22, as shown in Fig. 8. Each cavity consists of two etched-groove gratings and a single microstrip transducer. The two cavities are placed at a 90° angle and are coupled by a 45° obliquely oriented grating capable of deflecting the incident MSW beam by a 90° angle. The resonators reported in Ref. 22 exhibited insertion losses between 20 and 32 dB and a loaded Q value of 290 to 1570 over a tuning range of 2 GHz to 11 GHz.

The resonator structures discussed so far involve reflection surfaces or mirrors, which is complex in the sense that they require groove or metal-strip arrays to be fabricated on the YIG film surface. To avoid this complexity, it is also possible to directly use the straight edges of the YIG film to form an MSW cavity resonator. Figure 9 shows such a straight-edge resonator (SER) device, where the YIG/GGG resonator, which is of a rectangular shape cut by a dicing saw, is placed on top

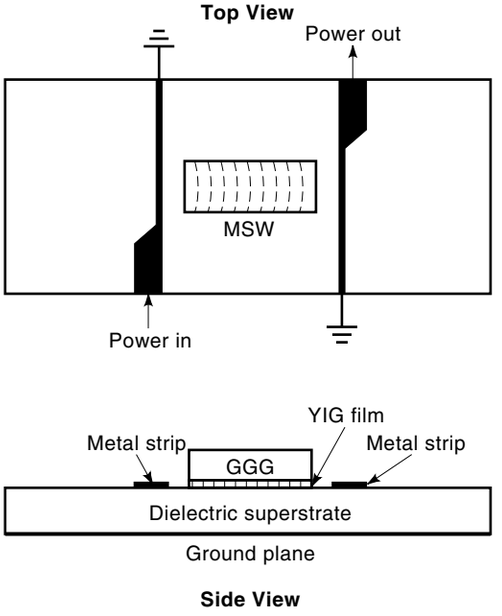

Figure 9. Schematic showing the configuration of a two-port MSW straight-edge resonator. The bias field can be applied perpendicular to the microstrip transducers in the YIG film plane or perpendicular to the YIG film plane for MSFVW or MSSW operation, respectively.

of the dielectric superstrate coupled in and out by the short-circuited microstrip transducers on both sides of the resonator. Depending on the bias field direction, both MSSW and MSFVW SERs can be constructed. Thus, MSSWs propagate along the surface of the YIG film and are reflected back onto the surface at the straight edges. A standing wave pattern results and a high-Q resonance is obtained. In this manner a MSSW SER was reported in Ref. 23, exhibiting an insertion loss of 3.1 dB and a sideband suppression level better than 20 dB tunable from 1 GHz to 22 GHz.

Finally, we consider the MSW structure of Fig. 10, which depicts a one-port resonator circuit. The circuit of Fig. 10 can be fabricated using photolithographic techniques, and, hence, cutting of reflective grooves on the YIG film is avoided. In Fig. 10, MSWs are excited within the metal window coupled in and out via the microstrip transducer. In order to form total reflection of the MSWs at the window boundary, and hence to achieve a high Q value, the geometry of the resonator needs to be carefully designed. The circuit of Fig. 10 allows for operation for all types of MSWs, and simple MSW resonators can be constructed.

MAGNETIC MICROWAVE NONLINEAR DEVICES

As discussed in the section entitled "Theoretical Background," nonlinear interaction terms arise from the equation of motion for the magnetization vector for which the small-signal assumptions no longer hold true. Under these conditions, the magnetization field will couple to itself, resulting in spin-wave interactions between different wave numbers and frequencies. In this section we discuss how this nonlinear phenomenon can be utilized for device applications. Among many important nonlinear devices, we will discuss frequency-selective limiters, signal-to-noise enhancers, amplitude correctors, and ferrimagnetic echoing devices.

Frequency-Selective Power Limiter

Frequency-selective limiters have been demonstrated using YIG spheres and ferrite slabs in the waveguide, coax, and stripline configurations (24). We will discuss here the limiter operation using a single-crystal yttrium–iron–garnet (YIG) film arranged in the configuration shown in Fig. 3, except that a meander line is normally used instead of a straight microstrip line. Also, a thick YIG film is preferred, because it implies an abundant spin-wave spectrum allowing the guided electromagnetic waves to react sufficiently with spin waves to induce instability at high power. All types of ferrite frequency-selective limiters operate analogously: When a transmission line is loaded with a ferrite element, the transmitted power cannot exceed a threshold value beyond which catastrophic energy transfer occurs between the guided RF electromagnetic fields and the spin precessing motion. This phenomenon has been discussed in the section entitled "Theoretical Background," and it is generally known as *Suhl's spin-wave instability* (12). Figure 11 depicts a simple picture explaining the operation of a frequency-selective power limiter.

We note that Suhl's spin-wave instability occurs when the RF field is perpendicular to the dc bias field. However, in some limiter applications the instability can also be induced by an RF field component parallel to the dc field. Spin-wave instability of this kind is known as parallel pumping, which, similar to Suhl's first-order instability, occurs at a magnon frequency one-half the frequency of the RF-pumping signal, $\omega_k = \omega/2$. The threshold for parallel pumping is

$$h_{\mathrm{P}}^{\mathrm{th}} = 2\Delta H_k \frac{\omega}{\omega_m} \tag{53}$$

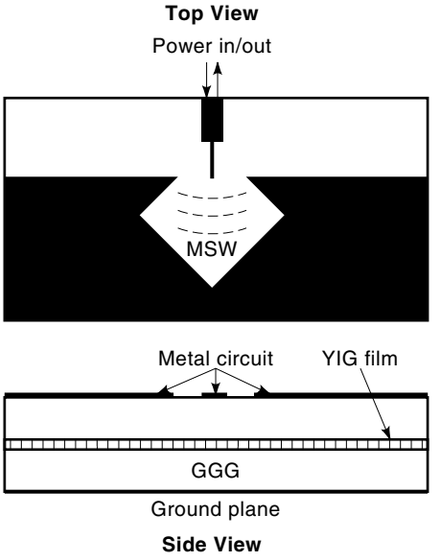

Figure 10. Schematic showing the configuration of a one-port MSW groove-free resonator. The bias field can be applied either perpendicular to the microstrip transducer in the YIG film plane, or perpendicular to the YIG film plane for MSFVW or MSSW operation, respectively.

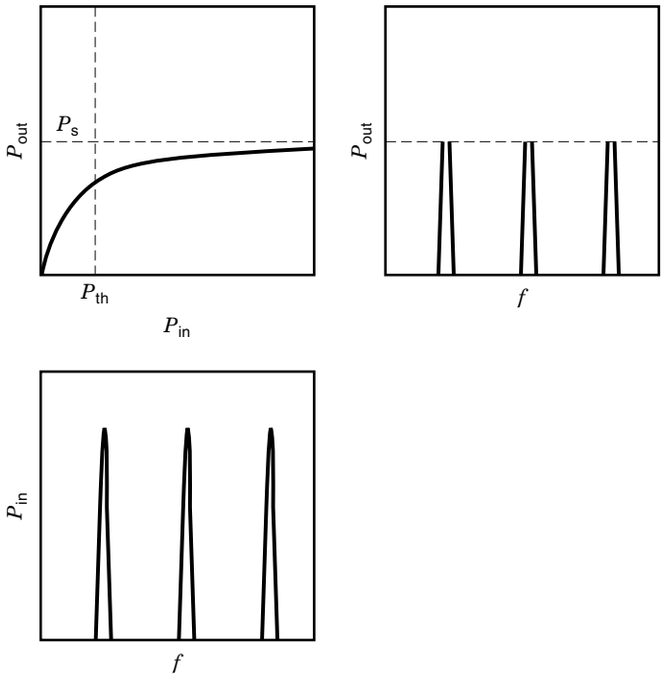

Figure 11. Power transmitted through a nonlinear frequency selective limiter. Input power spectrum is shown at the bottom left, and the output power spectrum is shown at the top right. The relationship between the input and the output powers is shown at the top left.

which compares closely in magnitude to h_d^{th}, the threshold for Suhl's first-order instability shown in Eq. (48).

As shown at the top left of Fig. 11, the relationship between the input power, P_{in}, and the output power, P_{out}, is roughly linear only when P_{in} is smaller than P_{th}, the threshold power. When P_{in} is larger than P_{th}, P_{out} becomes gradually saturated at $P_{s,}$ and the excess power, $P_{in} - P_{out}$, couples into spin-wave motion to be ultimately converted into lattice vibration and hence dissipated as heat. Thus, when P_{in} is given as a function of frequency, as shown at the bottom left of Fig. 11, the excess power of $P_{in} - P_{th}$ will be removed by the limiter; the resultant output characteristic is shown at the top right of Fig. 11. We note that Fig. 11 only shows an idealized operation. In reality the P_s level shown in the P_{out} versus P_{in} diagram is not a constant; it increases slightly with P_{in} when P_{in} exceeds P_{th}. As such, instead of showing chopped-head peaks, the output will consist of rounded-head transmission peaks in the P_{out} versus f diagram shown in Fig. 11.

As an example, in Ref. 25 a 57 μm thick YIG film was coupled to a 25 μm wide microstrip meander line of characteristic impedance 50 Ω fabricated on a high dielectric constant substrate. This limiter, which operated in the 2 GHz to 4 GHz range, showed a limiting range of 25 dB, a threshold input power level of 0 dBm, and a small signal loss of 7 dB. The upper frequency limits were not sharply defined, since the limiting power decreased with increasing frequency, but operation up to 8 GHz is possible with the present device.

The reason that the limiter device reported in Ref. 25 failed to operate at high frequencies can be explained in terms of the onset condition giving rise to Suhl's spin-wave instabilities. As discussed in the section entitled "Theoretical Background," Suhl's first-order instability occurs for spin waves possessing a frequency one-half the applied RF frequency. Thus, above 8 GHz, instability will occur in the spin waves of frequencies larger than 4 GHz, which are located above the spin-wave manifold extending the frequency range from 2 to 4 GHz. The second-order spin-wave instability, which involves spin waves of the same frequency as the applied RF signals, has a higher threshold and is not used in frequency-selective power limiters. Thus, a power limiter is operational only when half the applied frequency falls within the spin-wave manifold region bounded by the two frequencies ω_1 and ω_2 shown in Fig. 1. Since ω_1 and ω_2 can be tuned by varying the applied field strength, the limiter is therefore termed a frequency-selective device.

Signal-to-Noise Enhancers

Epitaxially grown single-crystal YIG films have been used to fabricate frequency-selective limiters and signal-to-noise enhancers. Although the construction of these two devices is very similar, as shown in Fig. 3, they perform opposite signal processing functions. The limiter presents low attenuation to low-intensity signals and high attenuation to high-intensity signals while the signal-to-noise enhancer attenuates weak signals more severely than strong signals. However, the major difference results from the origin of nonlinearities admitting the operation of these two devices. For a limiter the nonlinear coupling is related to the onset of spin-wave instabilities, whereas the nonlinear behavior of a signal-to-noise enhancer comes from the generation of magnetostatic waves (MSWs). The occurrence of the latter is at a much lower power level than that of the former.

Although a power limiter and a signal-to-noise enhancer are constructed using similar configuration as shown in Fig. 3, they are operating under different physical principles. While the former device requires the insertion loss to increase with input power, the latter requires the insertion loss to decrease with input power. A power limiter circuit will couple most efficiently with spin waves, whereas a signal-to-noise enhancer will avoid this by operating at a frequency ω so that $\omega/2$ is located well beyond the spin-wave manifold region. On the contrary a signal-to-noise enhancer will couple tightly with magnetostatic waves, for example, MSSW, while for a power limiter it is generally not the case. As a result, meander lines are therefore commonly used in power limiter circuits.

Let us examine the configuration of Fig. 3. Here we assume that the biasing magnetic field is applied parallel to the microstrip direction such that MSSWs are excited propagating perpendicular to the strip. Since the generation of MSSW in this configuration is very efficient, the input RF power is almost entirely consumed for the generation of MSSWs at low input-power levels. However, as the input power increases, the amplitudes of MSSWs increase accordingly until reaching saturation beyond which no more conversion into MSSWs is appreciable. Figure 12 shows that P_{MSSW} increases with the input power, P_{in}, linearly in the initial region but saturates at large P_{in}. The functional dependence of P_{MSSW} is similar to that of the output power from a limiter device shown in Fig. 11. The output power from the signal-to-noise enhancer is $P_{in} - P_{MSSW}$, which is shown as the heavy line in Fig. 12. Thus, from Fig. 12 we conclude that weak signals will be damped more by the generation of MSSWs than strong signals.

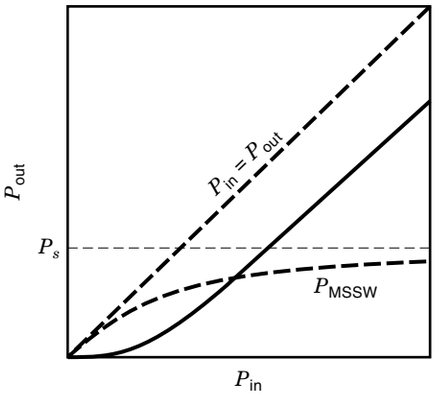

Figure 12. The relationship between the input power, P_{in}, and the output power, P_{out}, of a signal-to-noise enhancer. The converted MSSW power, P_{MSSW}, is also shown, and $P_{out} = P_{in} - P_{MSSW}$.

In Fig. 13 the top diagram shows the power spectrum output from a signal-to-noise enhancer device based on the input spectrum shown at the bottom of the figure. It is seen in Fig. 12 that noises, appearing at low power levels, are damped out, leaving alone the high level signals with improved signal-to-noise ratio. Again, Fig. 12 shows an idealized situation that P_s does not depend on the input power level, P_{in}. In reality, P_s will increase slightly with P_{in} when saturation is approached. As an example, Ref. 26 shows a signal-to-noise enhancer device centered at 3.3 GHz with a bandwidth of 800 MHz which exhibited 16 dB less attenuation when the input power is increased from -6 to $+10$ dBm.

Amplitude Correctors

For signal processing at microwave frequencies, broad-band amplifiers are needed whose characteristics are desired to show linear dependence on the amplitude of the input signals. However, for most power amplifiers including microwave traveling wave tubes (TWTs) the amplification deteriorates at high power, resulting in reduced power amplification for high-power input signals. One possible way to resolve this problem is to compensate the input power with a corrector which attenuates more input power at low input-power levels. This is exactly the same characteristics that we have discussed for a signal-to-noise enhancer, and hence it can be equally used as an amplitude corrector device. It is shown in Ref. 27 that an amplitude corrector operated at 3 GHz with low and high signal suppression level of 4.2 and 1 dB, respectively, and the threshold power level was 100 mW. This device was equipped with an O-type TWT operating from 2.5 GHz to 3.6 GHz, and correct output characteristics have thus been obtained.

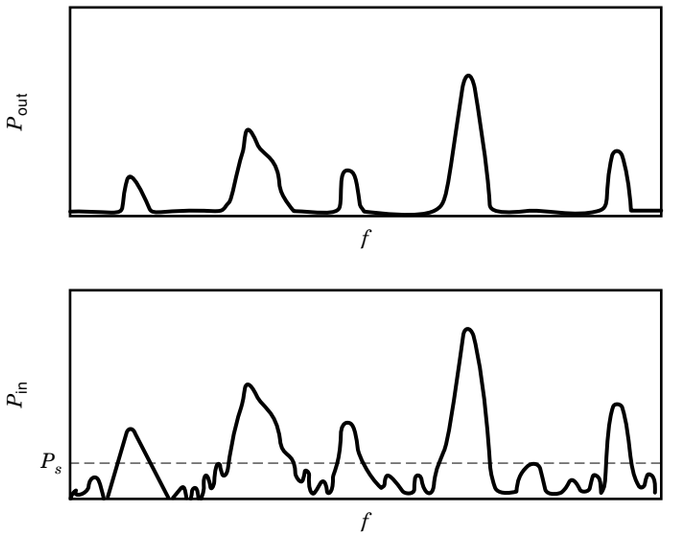

Figure 13. The input power spectrum (bottom) and the output power spectrum (top) applied to and transmitted from a signal-to-noise enhancer, respectively.

Nonlinear Ferrimagnetic Echoing Devices

Echo phenomena are characterized by the reradiation of the input signals stored in a nonlinear system through the agitation of a consequently applied pump pulse. Observation of ferrimagnetic echoes was first reported in 1965 by Kaplan in polycrystalline yttrium–iron–garnet (YIG) samples (28). Amplified echoes were thereafter reported in cylinders and truncated spheres of YIG crystals (29) and in single-crystal YIG films (30). Echo experiments offer a possibility of a novel approach to performing important signal processing functions, such as nondispersive time delay and pulse correlation in the frequency range below 10 GHz. With the demand of electronic technology advances there is now a renewed interest in the use of ferrimagnetic echoing devices.

Among many nonlinear systems capable of producing an echoed signal (e.g., cyclotron echo, plasma echo, molecular echo, phonon echo, and spin echo), only ferrimagnetic echo can show amplification. This feature renders the ferrimagnetic echo phenomena in a very unique position for device applications. Ferrimagnetic echo is mainly concerned with the reservoir of the electron spin system provided by a YIG crystal which is nearly the perfect medium for signal storage. That is, in view of the extremely narrow FMR linewidth (0.33 Oe at X band) the damping action accompanying the spin motion in the YIG crystal is very small; and once the spins are put in motion, they will continue the motion indefinitely in time exhibiting very little attenuation. The lifetime of the magnons in a YIG crystal is very long, usually exceeding 1 μs. We imagine that at the time instant $t = -\tau$ a signal pulse is applied to the YIG crystal setting the spins in precessing motion. Before the spin motion damped out, a pump pulse is applied at the time instant $t = 0$ which is so intense that nonlinear interaction is aroused in the spin system. Due to the (odd) cubic nature of the interaction, the process of time conjugation is recalled, which reverses the time scale for the stored signal such that the spins begin to precess in the opposite direction. As a consequence, at time $t = \tau$ (≤ 1 μs) the original signal pulse recovers, which appears as the image of the original signal echoed back by the pump pulse.

However, we must emphasize that if the cubic interaction is local in nature, no amplification is possible for the echoed signals, as occurs in the other nonlinear systems involving only isolated echoing sites. For ferrimagnetic echo the nonlinear interaction is brought about by the dipolar field interacting with the nonlocal spin waves showing a long-range dependence [this nonlocal interaction can be described in terms

of a Green's function whose kernel shows a $1/r$ dependence (31,32)]. As such, the echoed signal can get amplification, absorbing power from the pump pulse not only to restore the shape of the original signal, but also to amplify the signal to high intensity. The amplification gain can be as large as 100, as measured experimentally (28) and calculated theoretically.

Ferrimagnetic echo experiments are carried out using crystal YIG bulk or thin film materials in the presence of a high magnetic-field gradient (≈1 kOe/cm). In order to obtain high amplification gain the YIG material needs to be clamped between two polycrystalline poles to effectively suppress the demagnetizing field. Theoretically it has been demonstrated that the dc demagnetizing field has adverse effect in reducing the echo gain to zero (31,32). This result is consistent with Suhl's finding (12) that the dc demagnetizing field is apt to enhance spin-wave instability, resulting in subsidiary absorption during microwave resonance measurements.

Finally, we want to point out the similarities between the ferrimagnetic echo signals and the intermodulation noises observed in a ferrite circulator junction (33). Two RF signals at adjacent frequencies f_1 and f_2 will couple each other to form intermodulation noises at frequencies $2f_1 - f_2$ and $2f_2 - f_1$. Intermodulation signals grow rapidly with power, which may be identified as clicking noises in a telephone line. Actually, both the echoing signals and the intermodulation noises are generated through the same cubic interaction terms in the equation of motion. The only difference is that echo is a phenomenon in the time domain, whereas intermodulation is manifested in the frequency domain. While the dc demagnetizing field has been shown to have adverse effects in influencing the echo gain in the time domain, it has also been demonstrated that the same demagnetizing field will enhance the intermodulation level in a circulator junction (33). Therefore, the dc demagnetizing field needs to be suppressed or minimized in nonlinear studies concerning ferrite materials dealing with either the spin-wave instability, the echoing gain, or the intermodulation noises.

MAGNETOOPTIC DEVICES

At optical frequencies the Polder permeability tensor of a ferrite specimen is nearly isotropic with the diagonal element $\mu \approx 1$ and off-diagonal element $\kappa \approx 10^{-5}$, as can be calculated from Eqs. (11) and (12). Though small, the resultant magnetic anisotropy or gyrotropy can be measured using a laser optical beam. Upon incidence, the reflected and the transmitted beams will carry the magnetization information of the specimen, resulting not only in a rotation in polarization, but also in a change in reflectivity and transmission. This is called magnetooptic Kerr and Faraday effects for reflection and transmission measurements, respectively. Kerr and Faraday effects have been used in observing the dynamic processes of domain-wall motion in a ferromagnetic metal or a ferrimagnetic insulator sample, respectively (34).

The most important devices utilizing magnetooptic coupling for electronic signal processing applications concerns the scattering process between photons and magnons. This process is called Bragg diffraction, which in a ferrimagnetic medium a photon of momentum $\boldsymbol{P}$ is scattered by a magnon of momentum $\boldsymbol{k}$ to result in a photon of momentum $\boldsymbol{P} + \boldsymbol{k}$. This interaction is second order in nature and is described by the term $\gamma\mu_0 \boldsymbol{m}_k \times \boldsymbol{h}_P$ in Eq. (7). Here $\boldsymbol{m}_k$ denotes the magnetization field of the magnon and $\boldsymbol{h}_P$ is the magnetic field of the photon. As such, the photon wave is said to be modulated by the magnetization wave, carrying along with it the electronic information after scattering. Due to the nature of a second-order interaction, Bragg diffraction between photons and magnons, or MSWs in a magnetic film, is not very prominent, and only about 4% light diffraction was observed experimentally with a 7 mm interaction length for MSSW excitation approaching saturation (35).

Optical techniques are being increasingly utilized to meet the ever-growing data rate requirements of signal processing and communication applications. A key element to such applications has been acoustooptic modulators based on Bragg diffraction between photons and phonons. A large time-bandwidth product (TBW; i.e., time delay of acoustic signal in traversing the optical beam-times-signal bandwidth) is usually desirable. However, acoustic waves cannot be efficiently excited at frequencies above 2 GHz. Instead, magnetooptic devices offer the potential of large TBW modulation directly at microwave frequencies. The diffraction of guided optical waves by MSW is analogous to optical diffraction by a SAW and has the potential to enhance a wide variety of integrated optical applications such as spectrum analyzer, optical filters, deflectors, switches, and convolvers.

The basic theories of the MSW–optical interaction, including the development of expressions for optical diffraction efficiency and coupling factor as a function of the MSW power and other relevant parameters, has been derived in Ref. 35. The theory applies to the collinear configuration, shown in Fig. 14, with the MSW traveling in a direction parallel or antiparallel to the optical beam, as well as to the transverse configuration, shown in Fig. 15, where the MSW travels at an angle to the optical beam. In Figs. 14 and 15 prisms are used to guide optical beams onto the YIG layers which are transparent to light wave propagation. In Figs. 14 and 15 the MSW configuration may be replaced by the superstrate structure shown in Fig. 3. To achieve good optical properties the YIG film is usually highly doped, mainly by bismuth. As such, Bragg diffraction of guided optical waves by MSSWs and MSFVWs has been demonstrated in the configurations shown in Figs. 14 and 15, and the conversions between TE and TM

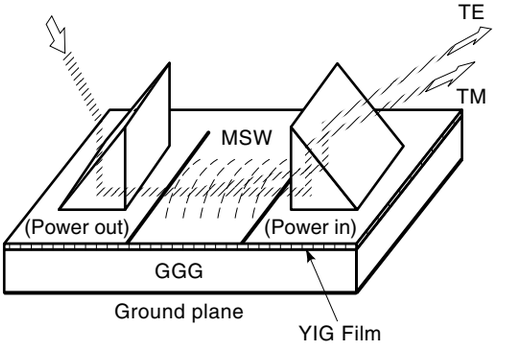

Figure 14. Collinear configuration with codirectional MSW and optical beams. Due to Bragg diffraction between the optical beam and the MSWs the original TM guided optical beam is scattered into a TE beam with deflected angle of propagation.

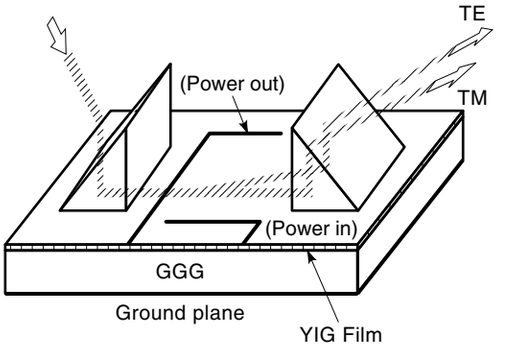

Figure 15. Transverse configuration for MSW and optical beams. Bragg diffraction of the guided optical wave by an MSW induces conversion between orthogonally polarized optical modes.

modes have been experimentally observed from 1 to 6.5 GHz (35).

These MSW-optical devices are currently in an early stage of development, with their basic feasibility having been demonstrated. However, they are expected to lead to a variety of high-performance integrated optical signal processing devices.

ANTIREFLECTION LAYERS AND ABSORBING LAYERS

To date, microwave or millimeter-wave antireflection layers and absorbing layers are almost exclusively used for radome design applications. Due to the highly classified nature of this topic, not much data have been published in the literature. In this section we discuss only the concepts that lead to the construction of microwave or millimeter-wave antireflection and absorbing layers. No explicit design parameters are given here. By definition, an antireflection/absorbing layer is to be placed on top of a substrate such that an incident microwave or millimeter wave beam will be totally transmitted/absorbed when passing across the layer without causing reflection. The layer shall be functional over a frequency range as wide as possible to be independent of the incident angle and polarization of the incident beam.

To realize the design of an antireflection layer, we consider first the case of normal incidence. According to the transmission line theory one concludes immediately that the first order solution would require the layer to behave as a quarter-wave transformer. This implies that the layer shall possess a thickness equal to one-quarter the wavelength with a characteristic impedance

$$Z_L = (Z_0 Z_S)^{1/2} \tag{54}$$

where

$$Z_0 = (\mu_0/\epsilon_0)^{1/2} \tag{55}$$

$$Z_S = (\mu_S/\epsilon_S)^{1/2} \tag{56}$$

Z_0 (Z_S) is the characteristic impedance of air (substrate), and ϵ_0 (ϵ_S) and μ_0 (μ_S) are the permittivity and permeability of air (substrate), respectively. When wider bandwidth is desired, higher-order solutions are required, and this results in a multilayer system with progressively changing electromagnetic parameters matching the impedance difference between air and substrate.

For an absorbing layer design the air impedance can also be matched by a multilayer system by progressively increasing damping parameters such that the series of the layers satisfies the transformer matching requirement. That is, we use the same impedance transformer theory for the design of absorbing layers, except that the impedances of the layers are now complex numbers, since the permittivity and permeability of the layers are complex numbers. As such, the incident wave damps out when it passes through the layer system before arriving at the substrate.

When oblique-angle incidence is considered, the impedance transformer theory can be generalized using the transfer matrix technique (36). The present problem becomes one of determining an optimal layer system design allowing for polarization-independent operation over as wide a frequency band and angle range on beam incidence as possible. Also, the design task is subject to a very important constraint requiring the thickness of the layers to be minimal, since at microwave and/or millimeter frequencies a practical layer system shall be thin enough compared with the wavelength in air. The design is in general not a trivial problem, and efficient computer algorithms are needed.

Once an optimal multilayer system is determined, the remaining task is to synthesize it using real materials. Unfortunately, nature does not provide general materials covering the whole range of electromagnetic parameters. Instead, artificial materials need to be developed. The first kind of artificial materials includes particle composites that contain dielectric particles (37), metal-shelled particles (38), and ferrite particles (39,40), and graphite powders are embedded in a matrix epoxy such that the effective permittivity, permeability, and/or conductivity of the composite can be controlled over the desired frequency range by adjusting the mixing fraction of the particles.

The second class of artificial materials is quite new; it involves periodic patterns of metal strips or grooves (surface relief gratings) to be fabricated on top of a layer surface. In fact when electromagnetic waves interact with periodic structures much finer than the wavelength, they do not diffract, but instead reflect and transmit as if they are encountering a nonstructured medium. Effective field theory describes the interaction between electromagnetic waves and such subwavelength structures by representing a region of subwavelength heterogeneity in terms of a homogeneous material possessing a single set of effective electromagnetic parameters: permittivity, permeability, and conductivity (41). Actually, the antireflection structures consisting of surface relief gratings can be found on the cornea of certain night-flying moths, and the first scientists investigating antireflection structured surfaces for application in the visible or near infrared portion of the spectrum worked to replicate moth eye surfaces (42).

BIBLIOGRAPHY

1. B. Lax and K. J. Button, *Microwave Ferrites and Ferrimagnetics,* New York: McGraw-Hill, 1962.

2. J. C. Slater, *Quantum Theory of Matter,* 2nd ed., New York: McGraw-Hill, 1972.
3. H. How, R. C. O'Handley, and F. R. Morgenthaler, Soliton theory for realistic domain wall dynamics, *Phys. Rev. B,* **40** (7): 4809, 1989.
4. C. Vittoria, *Microwave Properties of Magnetic Films,* World Scientific, Singapore, 1993.
5. S. Chikazumi and S. H. Charap, *Physics of Magnetism,* New York: Wiley, 1964.
6. C. Kittel, *Introduction to Solid State Physics,* 4th ed., New York: Wiley, 1971.
7. F. R. Morgenthaler, Dynamic magnetoelastic coupling in ferromagnets and antiferromagnets, *IEEE Trans. Magn.,* **MAG-8**: 130 (1972).
8. H. How and C. Vittoria, Surface retarded modes in multilayered structures: parallel magnetization, *Phys. Rev. B,* **39** (10): 6823, 1989.
9. H. How and C. Vittoria, Bulk and surface retarded modes in multilayered structures: antiparallel magnetization, *Phys. Rev. B,* **39** (10): 6831, 1989.
10. R. E. Collin, *Foundations for Microwave Engineering,* New York: McGraw-Hill, 1966.
11. C. Vittoria and N. D. Wilsey, Magnetostatic wave propagation losses in an anisotropic insulator, *J. Appl. Phys.,* **45**: 414, 1974.
12. H. Suhl, The theory of ferromagnetic resonance at high signal powers, *J. Phys. Chem. Solids,* **1**: 209, 1957.
13. V. L. Taylor, J. C. Sethares, and C. V. Smith, Jr., MSW terminations, *Proc. IEEE Ultrasonic Symp.,* 562, 1980.
14. M. R. Daniel, J. D. Adam, and T. W. O'Keeffe, Linearly dispersive delay lines at microwave frequencies using magnetostatic waves, *Proc. IEEE Ultrasonic Symp.,* 806, 1979.
15. K. W. Chang, J. M. Owens, and R. L. Carter, Linearly dispersive delay control of magnetostatic surface wave by variable groundplane spacing, *Electron. Lett.,* **19**: 546, 1983.
16. F. R. Morgenthaler, Field gradient control of magnetostatic waves for microwave signal processing applications, *Proc. RADC Microwave Magn. Workshop,* 133, 1981.
17. L. R. Adkins and H. L. Glass, Dispersion control in magnetostatic delay lines by means of multiple magnetic layer structures, *Proc. IEEE Ultrasonic Symp.,* 526, 1980.
18. W. S. Ishak and K. W. Chang, Magnetostatic wave devices for microwave signal processing, *Hewlett-Packard J.,* 10, 1985.
19. J. D. Adam, An MSW tunable bandpass filter, *Proc. IEEE Ultrasonic Symp.,* 157, 1985.
20. J. P. Castera and P. Hartemann, Adjustable magnetostatic surface wave multistrip directional coupler, *Electron. Lett.,* **16**: 195, 1980.
21. J. P. Castera, New configurations for magnetostatic wave devices, *Proc. IEEE Ultrasonic Symp.,* 514, 1980.
22. J. P. Castera and P. Hartemann, A multipole magnetostatic wave resonator filter, *IEEE Trans. Magn.,* **MAG-18**: 1601, 1982.
23. K. W. Chang and W. S. Ishak, Magnetostatic forward volume waves straight-edge resonators, *Proc. IEEE Ultrasonic Symp.,* 473, 1986.
24. G. S. Uebele, Characteristics of ferrite microwave limiters, *IEEE Trans. Microw. Theory Tech.,* **7**: 18, 1959.
25. S. N. Stizer and H. Goldie, A multi-octave frequency selective limiter, *IEEE MTT-S Dig.,* 326, 1983.
26. J. D. Adam and S. N. Stizer, A magnetostatic signal to noise enhancer, *Appl. Phys. Lett.,* **36**: 485, 1980.
27. W. S. Ishak, E. Reese, and E. Huijer, Magnetostatic wave devices for UHF band applications, *Circuits Syst. Signal Process.,* **4**: 285, 1985.
28. D. E. Kaplan, Magnetostatic mode echo in ferromagnetic resonance, *Phys. Rev. Lett.,* **14** (8): 254, 1965.
29. D. E. Kaplan, R. M. Hill, and G. F. Herrmann, Amplified ferrimagnetic echoes, *J. Appl. Phys.,* **40** (3): 1164, 1969.
30. F. Bucholtz, D. C. Webb, and C. W. Young, Jr., Ferrimagnetic echoes of magnetostatic surface wave modes in ferrite films, *J. Appl. Phys.,* **56** (6): 1859, 1984.
31. H. How and C. Vittoria, Theory on amplified ferrimagnetic echoes, *Phys. Rev. Lett.,* **66** (12): 1626, 1991.
32. H. How and C. Vittoria, Amplification factor of echo signals in ferrimagnetic materials, *IEEE Trans. Microw. Theory Tech.,* **MTT-39**: 1828, 1991.
33. H. How, T.-M. Fang, C. Vittoria, and R. Schmidt, Nonlinear intermodulation coupling in ferrite circulator junctions, *IEEE Trans. Microw. Theory Tech.,* **MTT-45**: 245, 1997.
34. J. M. Florczak and E. D. Dahlberg, Detecting two magnetization components by the magneto-optical Kerr effect, *J. Appl. Phys.,* **67**: 7520, 1990.
35. A. D. Fisher, Optical signal processing with magnetostatic waves, *Circuits Systems Signal Process.,* **4**: 265, 1985.
36. H. How, W. Hu, and C. Vittoria, Planar circuits in stratified dielectric/magnetic layered structures—An application to a slot line fabricated on a ferrite substrate, *IEEE Trans. Microw. Theory Tech.,* 1997, to be published.
37. L. Rayleigh, On the influence of obstacles arranged in rectangular order upon the properties of a medium, *Philos. Mag.,* **34**: 481, 1982.
38. H. How, W. A. Spurgeon, and C. Vittoria, The Microwave Properties of Conducting Spherical Shells, Technical Report, U.S. Army Materials Technology Laboratory, MTL TR 90-7, February 1990.
39. H. How and C. Vittoria, Demagnetizing energy and magnetic permeability tensor of spheroidal magnetic particles dispersed in cubic lattices, *Phys. Rev. B,* **43** (10): 8094, 1991.
40. H. How and C. Vittoria, The polder tensor of spherical magnetic particles in cubic lattices: An exact solution in multipole expansion, *Phys. Rev. B,* **44** (17): 9362, 1991.
41. D. H. Raguin and G. M. Morris, Antireflection Structured Surfaces for the Infrared Spectral region, *Appl. Opt.,* **32**: 1154, 1993.
42. P. B. Clapham and M. C. Hutley, Reduction of lens reflection by the 'moth eye' principle, *Nature (London),* **244**: 281, 1973.

HOTON HOW
ElectroMagnetic Applications